Eur. Phys. J. Plus (2015) **130**: 231
DOI 10.1140/epjp/i2015-15231-1

THE EUROPEAN PHYSICAL JOURNAL PLUS

Review

Evaluation of uptake and distribution of gold nanoparticles in solid tumors*

Christopher G. England[1,2,a], André M. Gobin[3,b], and Hermann B. Frieboes[1,2,3,c]

[1] Department of Pharmacology & Toxicology, University of Louisville, Louisville, KY 40292, USA
[2] James Graham Brown Cancer Center, University of Louisville, Louisville, KY 40292, USA
[3] Department of Bioengineering, University of Louisville, Louisville, KY 40292, USA

Received: 10 June 2015 / Revised: 10 September 2015
Published online: 19 November 2015 –

Abstract. Although nanotherapeutics offer a targeted and potentially less toxic alternative to systemic chemotherapy in cancer treatment, nanotherapeutic transport is typically hindered by abnormal characteristics of tumor tissue. Once nanoparticles targeted to tumor cells arrive in the circulation of tumor vasculature, they must extravasate from irregular vessels and diffuse through the tissue to ideally reach all malignant cells in cytotoxic concentrations. The enhanced permeability and retention effect can be leveraged to promote extravasation of appropriately sized particles from tumor vasculature; however, therapeutic success remains elusive partly due to inadequate intra-tumoral transport promoting heterogeneous nanoparticle uptake and distribution. Irregular tumor vasculature not only hinders particle transport but also sustains hypoxic tissue kregions with quiescent cells, which may be unaffected by cycle-dependent chemotherapeutics released from nanoparticles and thus regrow tumor tissue following nanotherapy. Furthermore, a large proportion of systemically injected nanoparticles may become sequestered by the reticuloendothelial system, resulting in overall diminished efficacy. We review recent work evaluating the uptake and distribution of gold nanoparticles in pre-clinical tumor models, with the goal to help improve nanotherapy outcomes. We also examine the potential role of novel layered gold nanoparticles designed to address some of these critical issues, assessing their uptake and transport in cancerous tissue.

Introduction

Nanotechnology has garnered tremendous research attention in the past two decades. In particular, gold nanoparticles (NPs) have been extensively studied for targeted cancer diagnosis, imaging, photohermal therapy, and drug delivery. Gold NP shape configurations have been various, including nanospheres, nanorods, nanocages, and nanoshells. Issues such as tumor targeting efficacy, pharmacokinetics and pharmacodynamics, toxicity, and biocompatibility have unfortunately hindered clinical application. Even if these issues were resolved, however, the abnormal structure of cancerous tissue presents serious challenges to effective nanotherapy. We review recent studies specifically focusing on overcoming tumor tissue transport barriers, first summarizing the main biological and physiological barriers to NP transport, then giving a brief overview of gold nanospheres and nanoshells and their construction, followed by a description of *in vitro* and *in vivo* experimental techniques to evaluate NP uptake and distribution in cancerous tissue. We then review gold NP uptake and distribution in 3D cell culture and *in vivo* animal studies, as well as recent computational modeling designed to complement the experimental analysis of NP transport in cancerous tissue.

Biological and physiological barriers to nanoparticle transport

Upon systemic injection, NPs first have to navigate the body's circulation while avoiding sequestration by the reticuloendothelial system (RES), which as part of the immune system is designed to remove pathogenic entities from

* Contribution to the Focus Point on "The Physics of Cancer" edited by M. Ben Amar.

[a] *Currently at*: Department of Radiology, University of Wisconsin School of Medicine and Public Health, E3/366 Clinical Science Center, 600 Highland Avenue, Madison, WI 53792, USA.
[b] *Currently at*: Texas Petrochemicals Inc., One Allen Center, Suite 1000, Houston, TX 77002, USA.
[c] e-mail: hbfrie01@louisville.edu

the body. The RES, first reported by [1], comprises a network of cells and tissues throughout the body, including in the blood, lymph nodes, liver, spleen, lungs, bone marrow, and connective tissue. Surface modifications are typically applied to NPs to minimize RES sequestering while pursuing passive and active targeting to tumor cells. In particular, coating with the hydrophilic polymer poly(ethylene)-glycol (PEG) has been shown to prolong circulation and avoid RES uptake [2,3], while promoting extravasation from tumor capillaries and diffusion in tumor tissue [4, 5]. PEG is currently the most widely employed FDA-approved polymeric platform for treating various cancers and related diseases, including Oncaspar for acute lymphoblastic leukemia, Genexol-RM for metastatic breast cancer, and Neulasta for chemotherapy-associated neutropenia [6]. While PEGylation enhances drug delivery, adverse effects have included potential immunogenicity, which is still controversial [7]. Coating of NPs with ligands specific for receptors over-expressed in cancer cells (such as the high-density lipoprotein receptor, HDLR) has also been shown to enhance NP uptake and accumulation in tumor tissue [3].

Cancer cells typically exhibit unscheduled proliferation resulting in tissue growth with inadequate vascular supply. The resulting hypoxia triggers angiogenesis [8–10], which is malfunctional due to uncoordinated stimulation from tumor cells [11,12], leading to irregular and leaky vessels [13], with pore sizes larger than normal (typically $\sim 400\,\text{nm}$ [14,15]). Consequently, appropriately sized NPs administered systemically can preferentially leak out of tumor vessels through the enhanced permeability and retention (EPR) effect [16–19]. NP transport and accumulation can be further affected by NP surface charge, morphology, and size [20,21].

The irregular tumor vasculature hinders therapeutic efficacy even if NP systemic travel and targeted accumulation were successful [22]. Tumor cells distant from vasculature are exposed to lower levels of diffusible substances (such as glucose, oxygen, NPs, and drug molecules) [23–27]. Hypovascularization promotes cells that invoke survival mechanisms to overcome low nutrient and oxygen conditions, including cell cycle arrest (quiescence) leading to cell cycle-dependent chemotherapeutic resistance [23,28–30]. Transport may be further hindered by an acidic microenvironment, increased interstitial fluid pressure (IFP), and a dense and disorganized extra-cellular matrix (ECM) [4,22,31–33]. As a result, cancer tissue may have almost twice the volume of interstitial space compared to normal tissue [23,26]. These biological and physiological barriers, coupled with intrinsic cellular resistance mechanisms, are a major reason underlying NP inefficacy to treat tumor tissue.

Gold nanoparticles as therapeutic agents

Physics- and engineering-based approaches have been applied to help address NP transport barriers. NPs can be constructed of inorganic or organic materials, or a combination of both. In particular, metallic NPs have been shown useful in various applications including *in vivo* imaging, photothermal therapy, and drug delivery. NPs have been synthesized from metals such as gold [34–39], silver [40–43], copper [44–46], palladium [47], ruthenium [48], or nickel [49–51]. Gold NPs have undergone extensive research, and they have been shaped in various ways and functionalized with moities for targeting cancer cell-specific receptors [52–54]. Previous studies have shown cellular uptake of gold NPs to be proportional to NP size [55–57]. Accordingly, NP size and surface modifications have been modulated in the quest to overcome transport barriers and deliver NPs more homogeneously into tumor tissue. Gold is an inert material, with NPs larger than 5 nm exhibiting little cytotoxicity [58,59] depending on the surface charge. Systemic toxicity can be further alleviated by coating with PEG, which can help hide the NPs from sequestering by the RES [20,59].

The clinical use of gold NPs has been hampered by poor biocompatibility and uncertain fate *in vivo* [60]. In lung cancer, for example, it was shown that gold NPs coated with 1-stearoyl-2-oleoyl-sn-glycero-3-phospho-(1′-rac-glycerol) were readily uptaken by lung adenocarcinoma cells, but they also seemed to induce lamellar bodies which could export the NPs out of the cell, thus generating acquired cell resistance [61]. Gold NPs have been effective in diagnosing lung cancer in exhaled breath by detecting elevated concentrations of volatile organic compounds [62] and through histological classification by binding to biomarkers of various lung cancer types [63].

Nanoshells are a special case of gold NP [64], composed of an outer metallic shell coating an inner core of a material such as silica, polystyrene, poly (lactic-co-glycolic) acid, or Fe_3O_4. In particular, silica-gold nanoshells have an outer gold shell with a dielectric silica core, and have been extensively studied for cancer applications [65,66]. Varying the thickness of the metallic shell enables optical tuning of nanoshells through their extinction spectra and hydrodynamic size. They can be designed to exhibit maximum absorbance in the near infrared (NIR)-spectral range, thus providing potential use for both photothermal therapy and multi-modality imaging. NIR-absorbing gold nanoshells have proven effective at reducing cell viability in solid tumors via hyperthermia when exposed to laser radiation [67,68].

Construction of gold NPs

To illustrate the physical process of gold NP construction, we describe as an example the methods employed in our previous work [69,70] to synthesize nanospheres and nanoshells.

Synthesis of gold nanospheres

Citrate-stabilized gold NPs are typically synthesized using a method in which chloroauric acid is reduced by trisodium citrate [71]. For example, 2.2–2.4 mL 1% wt/v citrate and 200 mL 0.01% wt/v $HAuCl_4$ are mixed and boiled for 10 min. The solution is then concentrated using a rotovapor to $\sim$ 20 mL. Although citrate-stabilized gold NPs may be easier for designing a system for transport modeling studies, they cannot be used for thermal ablation since the wavelength of light ($\sim$ 540 nm) required for activation will cause injury to live tissue. Their application is thus limited compared to silica-core gold nanoshells, which exhibit tunable optical properties and provide energy absorption in the NIR range required for photothermal ablation.

Synthesis of silica gold nanoshells

The synthesis of nanoshells consists of four steps: production of a colloid of small gold particles (2–4 nm) through reduction and aging of gold colloid following the recipe of Vogel *et al.* [72], fabrication of monodispersed silica cores via the Stöber method [73,74], attachment of the seeds to the silica surface, and gold shell growth via reduction of additional gold. The gold colloid solution is created using the THPC (Tetrakis(hydroxymethyl)phosphonium chloride) method [68]. Growth of the silica cores can be achieved via the combination of 7.5 mL tetraethyl-orthosilicate (TEOS), 225 mL absolute ethanol, and 12.5–13.5 mL ammonia. The ammonia is adjusted to achieve the desired silica core sizes. After removal of the paraffin cover and evaporation of the ammonia, the cores are coated with 3%–4% aminopropyltriethoxysilane (APTES). This allows for slightly positive cores for deposition of small colloidal gold particles, thus forming a seed particle. The seeds are washed and a 10% gold solution is added to complete the shell. After reaction time, the seeds are washed and re-dispersed in distilled water. The seeds are diluted to 0.3–0.5 optical density (OD) at 530 nm. A sweep is performed to optimize the chemical ratio between the seeds, K_2CO_3-$HAuCl_4$, and formaldehyde. Limiting the concentration of gold in the final reduction determines the thickness of the shell.

Functionalization of gold nanoparticles

In [69], gold nanospheres (45–60 nm) and silica gold nanoshells (160–175 nm) were functionalized with phosphatidylcholine (PC) and alkanethiol (two-layer), or high-density lipoprotein (HDL) and phosphatidylcholine/alkanethiol (three-layer), in the formation of layered NPs. The uptake and distribution of the layered NPs was evaluated in 3D cell cultures of various cancer cell lines, and their performance was compared to PEGylated NPs. PC is the most abundant phospholipid in the body and is a component of cell membranes, thus presenting less immunogenicity and offering an alternative to PEG. For example, PC has been used as a passivating agent for gold nanorods, significantly reducing their cytotoxicity [75]. Previous work has shown that thiol groups can help stabilize gold NPs due to the strong binding affinity between thiol and gold in comparison to the electrostatic binding with citrate [76–78]; a comprehensive review regarding the covalent interaction between gold and sulfur can be found in [78]. This functionalization creates a hydrophobic particle, with the thiol hydrocarbon chains pointing away from the core. Layering with the PC then yields a properly oriented layer surrounding the core as the hydrocarbon chains interact with the fatty acids of the PC. Such a two-layer approach may yield better biocompatibility as well as improved penetration into under-vascularized tumor tissue when compared to PEGylated particles. Additionally, the hydrophobic region between the PC and the thiol could potentially hold hydrophobic drugs.

In [69], the first layer applied to the gold nanospheres and silica-gold nanoshells was 1-Hexadecanethiol dissolved in ethanol. While stirring, 20 mL pure ethanol was placed in a beaker followed by 60 μL 1-Hexadecanethiol. The NPs were added to the sample slowly over the next few minutes. The sample was sonicated for 2 hours, and then placed for 12 hours on an orbital rocker. The sample was spun down at $5000 \times g$ for 15 min, and the pellet was washed twice with ethanol and sonicated before resuspension in 9 mL chloroform. The second functionalization was the addition of L-α-Phosphatidylcholine (PC). The stock solution was made by diluting the PC in chloroform (2 mg/mL), and 100 μL (molar ratio 2000 PC: 1 nanoparticle) was added to the particles coated with thiol and allowed to set for 12 hours on an orbital rocker. The solutions were transferred to glass tubes and the chloroform evaporated at ambient temperature. After removal of chloroform, PC-coated gold nanospheres and silica-gold nanoshells were reconstituted in ddH_2O to 2 OD. Three-layered particles were created by optimizing the ratio of HDL to NP optical density via an overnight reaction after 2 hours sonication. PEGylated NPs and nanoshells were created to compare their efficacy to the two- and three-layer NPs. To this end, 2000 MW PEG was added to gold nanospheres or nanoshells at a molar ratio of 2500:1. The solution was set on a rocker and allowed to react for 12 hours. Excess PEG was removed by centrifugation at $13000 \times g$ for 20 min, followed by resuspension in phosphate buffered saline (PBS).

Table 1. Layered Gold NP Characteristics (data from [69]). Two-layer includes coating with phosphatidylcholine (PC) and alkanethiol, while three-layer additionally includes high-density lipoprotein (HDL). Maximum wavelength was obtained using UV-Visible Spectroscopy, while size was evaluated via Scanning Electron Microscopy (SEM) and Dynamic Light Scattering (DLS, with hydrodynamic diameter representing z-average of the intensity distribution). Parentheses denote S.D. ($n = 3$).

Nanoparticle type	Functionalization	Max. wavelength (nm)	Diameter (nm) (via SEM)	Diameter (nm) (via DLS)
Gold nanospheres	PEGylated	533	52.6 (15.4)	82.81 (13.4)
	Two layer	540	47.1 (12.6)	74.91 (13.3)
	Three Layer	541	62.8 (14.9)	85.26 (18.7)
Silica gold nanoshells	PEGylated	820	146.2 (9.1)	161.82 (12.2)
	Two layer	855	144.9 (6.5)	155.11 (13.9)
	Three layer	860	158.1 (4.6)	169.41 (11.8)

Characterization of gold NPs

Gold NP surface modifications are typically assessed via optical, charge, and extinction spectra measurements (see table 1 for an example dataset). In [79] gold nanospheres had a peak absorbance in the range 533–541 nm, consistent with previous studies [80]. Size measured via scanning electron microscopy (SEM) was ~ 55 nm, while hydrodynamic size measured via DLS was ~ 80 nm. It has previously been shown that NPs sized ~ 50–60 nm can optimally recruit sufficient cellular receptors to induce cell internalization [81]. Further, gold NPs of this size have shown high uptake in orthotopic *in vivo* tumors [82]. In [79] silica-gold nanoshells had a peak absorbance in the range 820–860 nm, which corresponds to nanoshells with 110 nm diameter silica cores and ~ 15 nm gold coating [83]. With this set of parameters, the nanoshells exhibited ideal optical properties for NIR application [68,84].

The zeta potential of the NPs is measured in order to evaluate surface modifications. In [79], PC and thiol additions decreased the charge compared to PEGylated particles. In contrast, HDL increased the zeta potential to yield slightly negatively charged particles. PEGylated nanospheres had a zeta potential of -9 mV, while the two-layer version had -20 mV and the three-layer had -2 mV. In general, the nanoshells had higher surface charge than the nanospheres, due to the larger size of the nanoshells. The PEGylated versions had a zeta potential of -18 mV, the two-layer version had -29 mV, and the three-layer had -6.8 mV. These measurements were in agreement with previous studies [85–87].

Fourier Transform Infrared (FTIR) spectroscopy can be performed to ensure the presence of NP surface modifications. In [79], PEGylated NPs showed a C-O-C stretch of the PEG ether at $\sim 1050\,\mathrm{cm}^{-1}$ and vibration at $\sim 1350\,\mathrm{cm}^{-1}$, with -$CH_2$ and -CH_3 bending vibrations at $\sim 1450\,\mathrm{cm}^{-1}$. This stretch was smaller than previously observed [88], possibly due to the coating with PEG onto the silica-core nanoshells. The two-layer version with an outer layer of PC had ${PO_4}^{3-}$ group vibrations between ~ 820–$1000\,\mathrm{cm}^{-1}$, C-O-C stretch $\sim 1100\,\mathrm{cm}^{-1}$, with the largest band corresponding to the asymmetric and symmetric -CH_2 ($2880\,\mathrm{cm}^{-1}$) and -CH_3 ($2950\,\mathrm{cm}^{-1}$) stretch and vibration, respectively. The HDL-coated versions had asymmetric and symmetric -CH_2 ($2880\,\mathrm{cm}^{-1}$) and -CH_3 ($2950\,\mathrm{cm}^{-1}$) stretch and vibration, with C=O from the lipid ester $\sim 1750\,\mathrm{cm}^{-1}$, amide bonds in the range 1600–$1700\,\mathrm{cm}^{-1}$, and a phospholipid P=O_2 stretch $\sim 1250\,\mathrm{cm}^{-1}$. The two and three layers showed overlapping spectra possibly due to the layering process.

NP size and morphology can be determined via SEM (table 1). NP uptake into tissues has been shown to depend on particle shape [59]. In [79], nanoshells were observed to be spherical, as were most of the nanospheres, which is a desirable attribute to attain optimized optical properties for potential NIR therapy. PEGylated versions were mostly spherical measuring ~ 150–170 nm in diameter. Hydrodynamic size influences NP performance *in vivo*. Accordingly, dynamic light scattering (DLS) values are also usually measured. In [79], nanospheres were substantially smaller than nanoshells, measuring ~ 50 nm in diameter (table 1). Addition of hexadecanethiol and PC adds ~ 5–7 nm to the diameter due to the size of PC (~ 2.5–3 nm) and the –thiol (~ 2.5 nm) [89,90], while HDL adds ~ 10 nm [91].

Setup for experimental evaluation

The following provides examples of *in vitro* cell culture and *in vivo* animal experiments that have been typically used to assess gold NP uptake and distribution in tumor tissue. The detection of NPs using hyperspectral imaging is also described.

Cell culture and nanoparticle experiments in vitro

In [69], the gold NP performance was evaluated with three different types of cancer cell lines in tumor spheroid 3D cell culture: liver hepatocellular carcinoma (HEPG2), human lung adenocarcinoma (A-549), and pancreatic adenocar-

cinoma (S2VP10). The spheroids ranged between 0.5 and 2 mm in diameter, while the S2VP10 cells formed smaller, grape-like tumors. The spheroids were incubated with 40 μL NPs at 25 OD for 6 hours. Spheroids were allowed to set for 2 hours in cryomolds made of tissue freezing medium, and then sectioned in 5 μm slices for histological analysis.

Mouse model experiments in vivo

For the study in [70], severe combined immunodeficiency (SCID) female mice received an orthotopic pancreatic injection of S2VP10 metastatic pancreatic adenocarcinoma cells expressing luciferase, resulting in pancreatic tumors within 7 days. An intravenous (tail vein) injection of 200 μL 2 OD NP solution was given to each mouse 9 days after tumor cell implantation. As there were five mice in each cohort, the first cohort received an injection of PC-coated gold nanospheres; the second cohort received an injection of PC-coated silica-gold nanoshells, and the third cohort received no injection (negative control). NPs were allowed to circulate for 48 hours before mice were euthanized. The pancreatic tumor, liver, and spleen were removed from each mouse for histological processing, with the liver and spleen providing a measure of NP uptake by two major components of the RES.

NP detection using hyperspectral imaging

Silver enhancement staining can be used to detect gold NPs in tissue samples using brightfield microscopy, although the staining intensity also depends on particle size and shape in addition to particle number, thus providing a qualitative assessment. A more quantitative evaluation can be performed via scanning electron microscopy (SEM) or transmission electron microscopy (TEM); however, these techniques by themselves cannot conclusively detect NPs. Elemental analysis in combination with other techniques (such as energy dispersive X-ray (EDX) microanalysis) provides further confirmation of NP identity [92]. Other techniques for gold NP detection in tissue have included confocal microscopy [93], atomic force microscopy (AFM) [94], fluorescence microscopy [95], dark-field microscopy [96], reflectance imaging [93], photothermal interference contrast [97], and micro computed tomography (micro-CT) [98]. Recently, hyperspectral imaging in combination with dark-field microscopy was used in [69,70,99] to assess NP uptake and distribution within histology tissue sections. In this approach, spectral libraries of known NPs are created to enable their detection in tissue. The combination of hyperspectral imaging with dark-field microscopy thus enables automated NP detection. Previous work illustrates the use of this technology for NP detection in biological tissues. For example in lung cancer, the deposition patterns of cisplatin aerosol therapy in surgically resected stage II lymph nodes was analyzed using hyperspectral imaging [100]. Hyperspectral imaging was also used to analyze the morphology and particle distribution of liposomes encapsulating recombinant human epidermal growth factor [101]. This type of imaging has also been utilized in patients for rapid histological classification of lung cancer type [102].

The CytoViva Hyperspectral Imaging System uses a Dage camera with a microscope with dark-field capability. Hyperspectral profiles are acquired using a Pixelfly camera and visualized using ENVI 4.8 software. To confirm the identity of NPs, spectral libraries are created using z-spectral profiles and compared to the tissue samples. The spectral mapping is able to detect and confirm the NPs within tissue samples by using multiple tissue images (> 10) containing either NPs or no NPs. Data analysis can be performed with ImageJ. NPs are counted in various regions of tissue (*e.g.*, tumor spheroids [69,70] or multilayered cell cultures [99]) to determine concentration. However, light scattering from different components in dense tissue samples may hinder detection. Thus, to computationally extract the NPs, spectral matching should be mapped for each image to provide a clear identification of pixels associated with NPs. NP spectral profiles may be altered by backscatter from other sources, agglomeration status, and other mechanisms. For the tissue obtained from *in vivo* experiments, regions of interest can be randomly determined and particles within these regions counted to determine concentration. In this case, a sufficient number of regions should be evaluated to ensure an acceptable level of accuracy (*e.g.*, based on stereological analysis).

Evaluation of gold NP uptake in cell culture

Small gold NP uptake by cancer cells in monolayer, 3D cell culture, and tumors *in vivo* was assessed in [76]. Two NP sizes (50 and 100 nm) were coated with tiopronin, a thiol drug used to control the rate of cysteine precipitation and excretion in patients suffering from cystinuria [103]. Tiopronin can be used as a stabilizing agent for metal NPs because its thiol groups prevent NP agglomeration [104], while its carboxyl groups can be modified with peptides, molecules, or drugs. It was previously shown that tiopronin-coated NPs functionalized with targeted and therapeutic peptides evinced enhanced NP uptake and distribution in 3D cell cultures of MCF-7 human breast cancer cells and in mice *in vivo* [105].

Exposure to the tiopronin-coated NPs for 24 hours was not toxic to the MCF-7 cells, indicating good biocompatibility [76]. Human breast cancer MCF-7 cells were then treated with 50 and 100 nm NPs at a concentration of

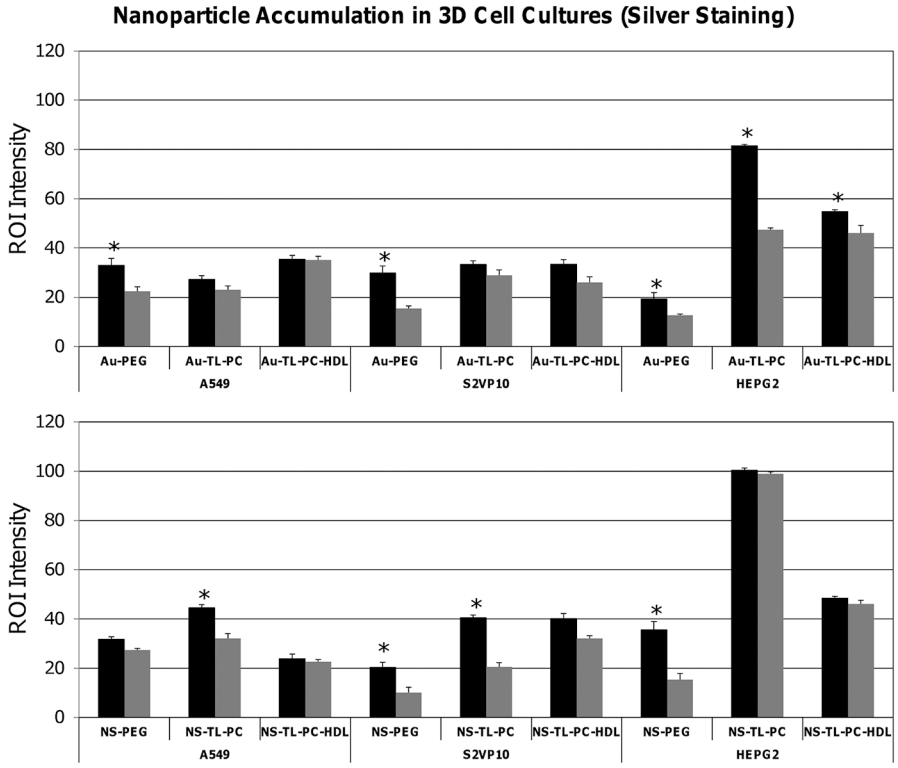

Fig. 1. Uptake of gold NPs in 3D cell culture measured via silver enhancement (data from [69]). Top: gold nanospheres; bottom; silica gold nanoshells. ROI intensity measurements are shown for peripheral (black bars) and inner regions (grey bars) of A549 (non-small cell lung cancer), S2VP10 (pancreatic), and HEPG2 (liver) 3D cell cultures. Peripheral regions generally showed equal or higher number of NPs than the interior. Error bars represent standard deviation from $n = 3$ measurements; asterisk indicates statistically significant difference ($p < 0.05$) evaluated with Student's t-test with $\alpha = 0.05$.

1 nmol/L for 24 hours. Comparison of the number of NPs in each cell *versus* NP size indicated that cellular uptake occurred in a size-dependent manner. More than 5× uptake was observed for the 50 nm compared to the 100 nm NPs, in agreement with a previously reported maximum uptake of 50 nm citrate-stabilized gold NPs [106]. The intracellular distribution of NPs after treatment was assessed by Bio-TEM, showing that both NP sizes localized in the cellular cytoplasm in an aggregated state. The density of 50 nm NPs was significantly higher than that of 100 nm NPs, which was in accordance with results from inductively coupled plasma mass spectrometry (ICP-MS).

In the 3D cell culture spheroid model, positively charged NPs were taken up mostly by proliferating cells [76], while negatively charged NPs were able to deliver their payload deeper into tissue due to fast diffusion [107]. Arginine-glycine-aspartic acid peptide-conjugated dendrimers were developed to enhance NP delivery into tissue. These dendrimers exhibited significantly enhanced penetration of dendrimer/siRNA NPs into U87 malignant glioma 3D cell cultures. The mechanism seems to be based on decreased integrin-binding affinity [108,109]. Accordingly, 50 and 100 nm tiopronin-coated gold NPs with the same surface properties were prepared, in order to assess the effect of size on tissue penetration. The 3D cell cultures were exposed to the NPs at a concentration of 1 nmol/L for 3 and 24 hours. Evaluation of HE staining with dark-field microscopy showed that at 3 hours the NPs were primarily located at the periphery of the spheroids [76]. The penetration of the 50 nm NPs increased with extended incubation time from 3 to 24 hours, the amount being about 4× higher than that of the 100 nm NPs. A corresponding size-dependent differential in NP concentration was also observed. These results are in agreement with previous work showing that NP penetration into spheroids is limited to NP sizes smaller than 100 nm [110]. Similarly, NPs sized ~ 20 nm showed better penetration into spheroids than larger NPs [110].

In another study [111], ultra-small gold (2 and 6 nm) NPs were shown to have superior uptake and penetration of MCF-7 breast cancer cells in monolayer, 3D cell culture, and tumors *in vivo* compared to larger (15 nm) NPs. The NP uptake in cells in monolayer and their penetration in tumor spheroids was inversely proportional to the NP size. Intriguingly, 2 and 6 nm NPs were found in both cell cytoplasm and nuclei *in vitro* and *in vivo*, while 15 nm NPs aggregated in the cytoplasm. The gold content increased significantly with incubation time from 3 to 24 hours for both 2 and 6 nm NPs, but not for the larger 15 nm NPs [111]. The 2 and 6 nm NPs were distributed throughout the spheroids, suggesting deep penetration by the smaller particles, while the 15 nm NPs were found mostly at the spheroid periphery. ICP-MS analysis demonstrated that the number of NPs detected in 3D cell culture was inversely

proportional to their size. This observation is consistent with previous work showing that NPs smaller than 20 nm have superior tissue penetration compared to larger (40, 100, or 200 nm) NPs [110].

In [69], tumor spheroid sections representing hypo-vascularized tumor tissue from three different cell lines (A549 non-small cell lung cancer, S2VP10 pancreatic adenocarcinoma, and HEPG2 liver cancer) were treated with silver enhancement staining to assess NP uptake and distribution after exposure to layered nanospheres or silica gold nanoshells. Region of interest (ROI) measurements were taken at the periphery and center of the spheroid cultures. Samples exposed to two- and three-layer nanoshells had higher ROI intensity than PEGylated versions for all three cell lines. For the A549 cell line, the three-layer nanospheres had more uniform distribution compared to the PEGylated version (fig. 1, top left). In contrast, an increased accumulation of two-layer compared to PEGylated nanoshells was observed for the A549 cell line (fig. 1, bottom left). The two-layer nanoshells had more of a differential between periphery and tumor interior compared to the three-layer case (fig. 1, bottom left). For the S2VP10 cells, all of the two- and three-layer particle versions had significantly higher ROI in the interior than the PEGylated versions, suggesting increased penetration (fig. 1, middle). A more uniform particle distribution was suggested by the two- and three-layer nanospheres, which presented similar ROI intensity values between spheroid periphery and interior compared to the PEGylated versions (fig. 1, top middle). Two- and three-layer nanoshells had $\sim 2\times$ the ROI intensity values at the periphery for the S2VP10 cell line compared to the PEGylated version (fig. 1, bottom middle), with the three-layer showing $\sim 50\%$ higher values in the interior compared to the two-layer.

For the HEPG2 cell culture, the two-layer nanospheres attained a peripheral ROI intensity almost $2\times$ that of the interior, indicating a steep diffusion gradient into the 3D culture (fig. 1, top right). In comparison, the three-layer nanoshells showed similar intensities between periphery and interior, and at similar values than the nanospheres, indicating more uniform but poorer penetration (fig. 1, right). The two-layer nanoshells had ROI intensity values statistically the same between the periphery and interior of the HEPG2 cell culture, indicating uniform distribution into the tissue. The particles had an ROI intensity nearly $2\times$ that of the three layer and $3\times$ that of the PEGylated versions (fig. 1, bottom). The PEGylated version had higher ROI intensity at the periphery than the interior while having the lowest particle uptake (fig. 1, bottom). The ROI intensities recorded for the HEPG2 cell line were higher than both the S2VP10 and A549 cell lines, indicating a higher number of particles uptaken in the HEPG2 cell culture for all particle types.

Application of spectral libraries for the detection of gold NPs

In [70], spectral libraries were created of PC-coated silica-gold nanoshells and nanospheres before detection in tissue samples. These libraries could later be matched to the tissue images for NP detection. In fig. 2, visible color changes (green to yellow to red) illustrate the shift of the maximum absorbance wavelength. The majority of nanospheres in solution exhibited green color, indicating maximum absorbance values within the lower range (500–600 nm) of the spectrum (fig. 2A). This was confirmed through the z-profile spectra mapping showing a maximum band at $\sim$ 550–570 nm. The nanoshells contained a significant concentration of red NPs, indicative of absorbance at higher wavelengths (> 700 nm) (fig. 2B).

Dark-field microscopy enables observation of the NPs within tumor spheroid histology sections [70]. The light reflected by the particles provides sharp contrast with the surrounding tissue, enabling counting of the particles. Figure 3 shows a representative image, displaying small red-orange dots indicating particles within the tissue. Hyperspectral mapping was used to filter out the tissue to highlight the NPs [112]. NPs were thus identified, and their uptake and distribution assessed within the samples (fig. 4). The three-layer nanospheres in the A549 tumors and the two-layer silica gold nanoshells in the HEPG2 tumors showed the best performance, in agreement with silver staining measurements. Both particle types behaved similarly in the S2VP10 tissue, evincing steeper diffusion gradients and lower uptake. The three-layer formulation showed slightly higher uptake in the S2VP10 tumors, possibly due to a looser morphology and to other pancreatic cell cancer-specific interactions with the HDL layer. Overall, the PEGylated particles had poorer penetration and lower uptake. Comparing the nanoshell performance across 3D cell cultures, the three-layer formulation exhibited an average 50% lower uptake compared to the two-layer [70]. The nanospheres had $\sim 30\%$ higher penetration at the spheroid periphery compared to the nanoshells, which may be mostly attributed to the larger size of the nanoshells ($3\times$ that of the nanospheres).

The penetration and uptake dynamics of gold NPs has very recently been studied using a Multilayered Cell Culture Model (MCL) [99], showing that NP transport and uptake are highly dependent on the tumor cell type. Gold NPs sized 20 nm were able to penetrate deeper into tissue composed of MDA-MB-231 cells than of tissue of MCF-7 cells, both human mammary carcinoma cell lines. The intracellular and extracellular spatial distribution of the NPs was mapped using hyperspectral imaging, illustrating the differential NP uptake between monolayer and tissue-like MCL models.

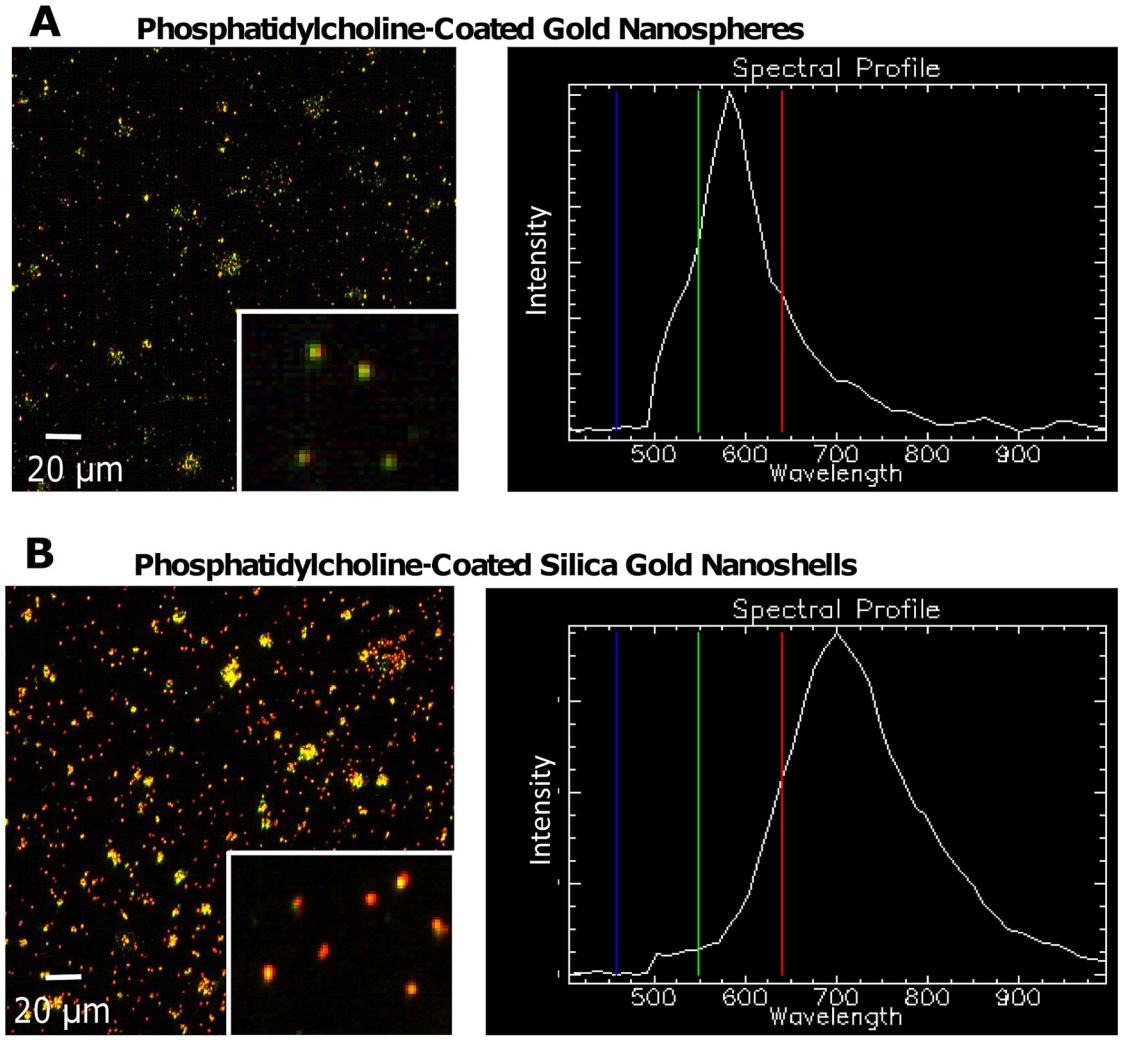

Fig. 2. Hyperspectral imaging of PC-coated gold NPs [70]. (A) Gold nanospheres were primarily green, with a spectral profile indicating a maximum wavelength of 570 nm. (B) Silica-gold nanoshells displayed an abundance of red and yellow, with a spectral profile maximum of 700 nm. While the actual maximum wavelength of silica-gold nanoshells in solution is 820–860 nm, hyperspectral imaging is known to underestimate entities containing higher wavelength maxima. Bar, 20 μm. Reprinted from England *et al.*, *PLoS One* **10**, e0129172 (2015); used in accordance with Creative Commons Attribution (CC BY) license.

Evaluation of gold nanoparticle uptake in vivo

Accumulation of NPs in an organ is primarily a function of the associated tissue vasculature. Both the spleen and liver are highly vascularized tissue and thus offer a high number of extravasation sites, while tumors with impaired vascular development offer limited extravasation sites. The accumulation of 50 and 100 nm gold NPs was evaluated in mice *in vivo* in [76]. The pharmacokinetic behavior was first investigated after a single 5 mg NP/kg intravenous injection, with the results showing that the NPs were rapidly eliminated from circulation: the NP concentration decreased to 11.0 μg/mL at 10 min and 1.9 and 0.2 μg/mL at 8 and 24 hours for the 50 nm NPs, respectively [76]. The 100 nm NPs were cleared faster from circulation than the 50 nm NPs. The pharmacokinetic behavior is affected by many variables, including NP size and surface properties influencing the extent of opsonization and clearance. Since the NPs were coated with tiopronin, they were easily opsonized and cleared from circulation. A higher amount of gold was detected at 24 hr post injection for the 50 nm NPs (0.42 μg/g) and less for the 100 nm NPs (0.14 μg/g) [76]. The NPs accumulated predominantly in the spleen and the liver, uptaking more than 80% of the injected dose. The spatial distribution of the NPs was observed to be heterogeneous within the tumor tissue, with most of the NPs apparently remaining in the vicinity of the blood vessels after extravasation.

Gold NP pharmacokinetics was investigated after a single intravenous dose of 5 mg NP/kg in mice *in vivo* [111], finding that the NPs were rapidly eliminated from circulation. The concentration of gold in the blood for 2 nm NPs was 26.2 μg/mL at 10 min post injection, 7.57 μg/mL at 8 hr, and 0.94 μg/mL at 24 hours. For 6 nm NPs, the

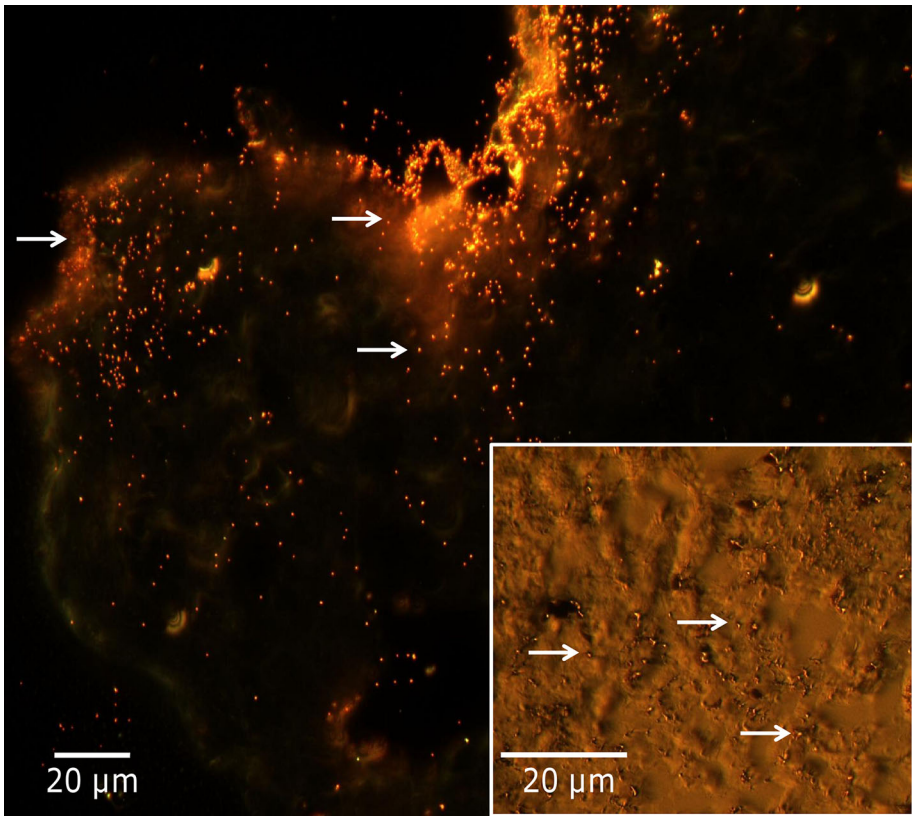

Fig. 3. Representative dark-field microscopy to assess gold NP uptake in 3D cell culture tissue histology, with hyperspectral imaging used to confirm particle identity (data from [69]). Image (60×) shows increased particle concentration around periphery of HEPG2 histology section (upper left), with a decreasing number towards the interior. Inset: Image of A549 histology section (100×) shows particles (arrows) distributed through the tissue.

corresponding levels were 9.0 μg/mL, 2.8 μg/mL, and 0.51 μg/mL. The larger 15 nm NPs were cleared even faster, since the coating with tiopronin enhanced opsonization and clearance from circulation. These results indicate that smaller NPs extravasate from circulation and diffuse in tissue easier than the larger NPs. It has been shown that NPs with the capability to "shrink" from 100 nm to 10 nm exhibit deep tumor penetration and high accumulation in tumors *in vivo* [113]. In another study, the delivery of NPs with 12 nm diameter was enhanced by vascular normalization in mammary tumors, whereas larger 125 nm NPs were hindered [114]. The 2 and 6 nm NPs were widely distributed in different organs of the body, accumulating preferentially in the kidneys and with smaller amounts detected in the spleen and the liver. This is consistent with the distribution of 1.9 nm NPs [115,116]. In contrast, $> 70\%$ of the injected dose of 15 nm NPs was found in the spleen and the liver [111].

Systemic gold NP uptake *in vivo* based on NP size was evaluated in [117]. The NPs were traced after 1, 4 or 24 hours post intravenous (IV) (2 or 40 nm NPs) or intraperitoneal (IP) (with 40 nm NPs) injection. The NPs were primarily detected in macrophages only, and at moderate exposure mainly in the Kupffer cells in the liver. The IV injections yielded rapid NP uptake by the Kupffer cells, followed by slower uptake by macrophages in the spleen. In contrast, the IP injections yielded delayed uptake in the liver along with a moderate uptake in macrophages at the spleen, small intestine, and mesenteric lymph nodes. The NPs were not found in other organs, including lungs, brain, adrenal glands, kidneys and ovaries, and placenta and fetal liver for pregnant subjects. The results indicate that inert gold NPs penetrate cell membranes by endocytosis. Further, independent of size, the NPs were mainly uptaken by Kupffer cells in the liver and secondarily by macrophages in other organs. The blood-brain barrier apparently prevents the NPs from penetration into the central nervous system. The 2nm NPs also seemed to be removed through urinary excretion via filtration in the renal glomeruli.

The uptake of a delivery system composed of 5 nm gold NPs loaded with cetuximab (C225) as a targeting agent, and gemcitabine as a chemotherapeutic drug was evaluated with an orthotopic pancreatic tumor growth *in vivo* using metastatic AsPC-1 cells [118]. Cetuximab is a monoclonal antibody that inhibits EGFR expressed on the cell surface of some cancers. The growth was monitored non-invasively via bioluminescence measurements, showing the advantage of a targeted system. Uptake of gold in various tissues was measured via inductively coupled plasma (ICP) analysis. The gold content in the tumor indicated that C225 was an efficient targeting agent, and showed that the loading with gemc-

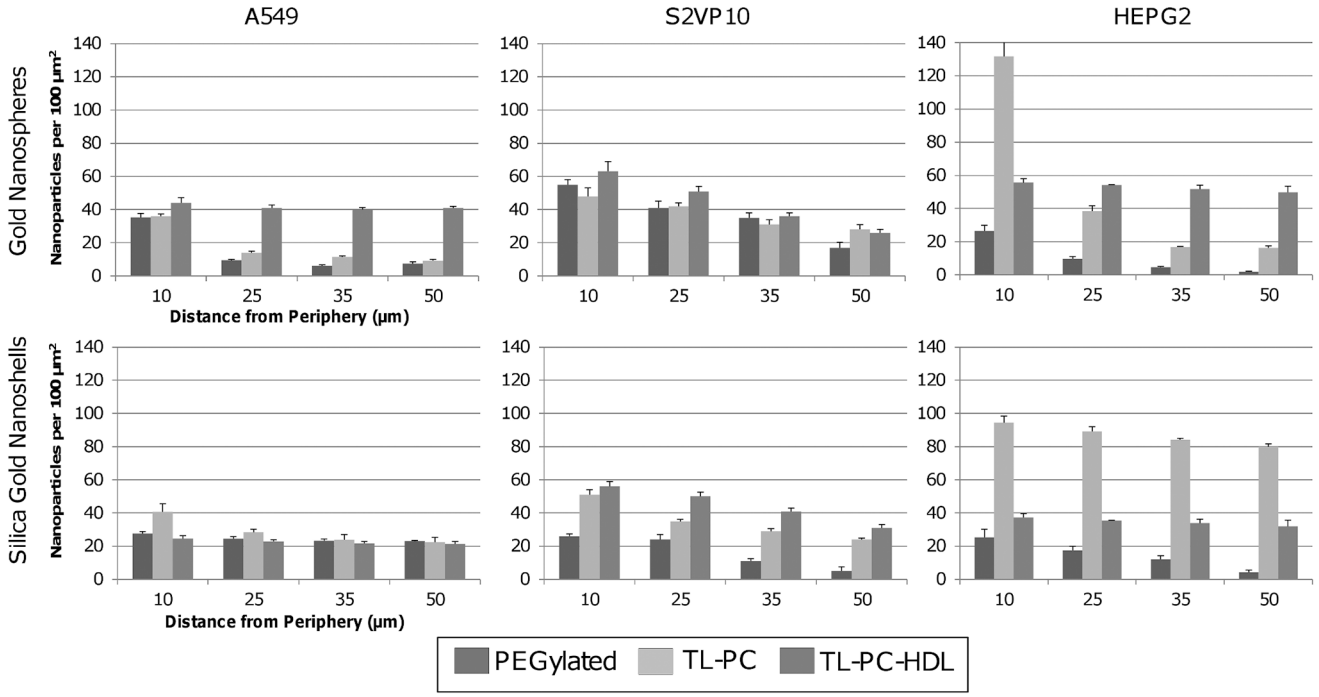

Fig. 4. Gold NP penetration and distribution in 3D cell cultures measured by dark-field microscopy (data from [69]). Particle uptake was measured as a function of distance from the tumor spheroid periphery for gold nanospheres (top) and silica gold nanoshells (bottom) for A549 (non-small cell lung cancer), S2VP10 (pancreatic), and HEPG2 (liver), 3D cell cultures. The three-layer gold nanospheres in the A549 tumors and the two-layer silica gold nanoshells in the HEPG2 tumors had the best performance, while both of these particle types behaved similarly in the S2VP10 culture, with steeper diffusion gradients and lower uptake. The PEGylated particles showed poorer penetration and lower uptake. All error bars represent standard deviation from at least $n = 3$ measurements.

itabine did not affect this targeting. Gold uptake by the liver and kidney was minimal, further highlighting the targeting efficacy. Treated tumors showed significant regression compared to untreated controls, with volumes reduced by $\sim 75\%$. These results were confirmed *in vitro* with three pancreatic cancer cell lines (PANC-1, AsPC-1, and MIA Paca2) having variable epidermal growth factor receptor (EGFR) expression [118]. The testing showed that gold uptake correlated with EGFR expression, while evaluation of efficacy indicated significant inhibition of cell proliferation *in vitro*.

The biodistribution and uptake of PC-coated gold nanospheres and silica gold nanoshells *in vivo* was examined in [70]. The NPs were tail-vein injected into mice bearing orthotopic pancreatic tumors to enable systemic evaluation. Using dark-field microscopy in combination with hyperspectral imaging applied to histology samples, NP counts were obtained in the vicinity of extravasation sites to assess the distribution and uptake in various organs and tissues, including liver, spleen, and tumor. For nanospheres, the spleen exhibited a higher uptake of 35.5 ± 9.3 particles/$100\,\mu\text{m}^2$ within $10\,\mu$m of the source, followed by an exponentially decaying penetration pattern which was limited to $\sim 50\,\mu$m (fig. 5). The liver and pancreatic tumor displayed a linear decline in concentration, with 26.5 ± 8.2 and 23.3 ± 4.1 particles/$100\,\mu\text{m}^2$, respectively, within $10\,\mu$m of the source and few NPs penetrating beyond $50\,\mu$m (fig. 5). NP concentration was highest in the liver (1.09 ± 0.14 NPs per μm^2) in comparison to the spleen (0.74 ± 0.12 NPs per μm^2) and pancreatic tumor (0.43 ± 0.07 NPs per μm^2).

In this same study [70], silica-gold nanoshells exhibited limited penetration beyond $30\,\mu$m in the spleen and pancreatic tumor (fig. 5), with uptake of 22.1 ± 6.2 and 15.8 ± 6.1 particles/$100\,\mu\text{m}^2$, respectively, within $10\,\mu$m. The nanoshells were uptaken mostly within the liver and displayed on average 31.1 ± 4.1 particles/$100\,\mu\text{m}^2$ within $10\,\mu$m of the nearest source, with penetration hindered beyond $30\,\mu$m (fig. 5). The nanoshells exhibited a decaying exponential pattern in the liver, spleen, and pancreatic tumor, implying limited diffusion possibly due to size. NP concentration in the liver was 0.43 ± 0.07 NPs per μm^2, and 0.30 ± 0.06 NPs per μm^2 and 0.20 ± 0.04 NPs per μm^2 in the spleen and the pancreatic tumor, respectively.

Evaluation of nanotherapy using computational modeling

In general, the large number of parameters available to tune NP performance coupled with the variability in tumor tissue makes it challenging to evaluate these complex interactions solely through experimental observation. Hence,

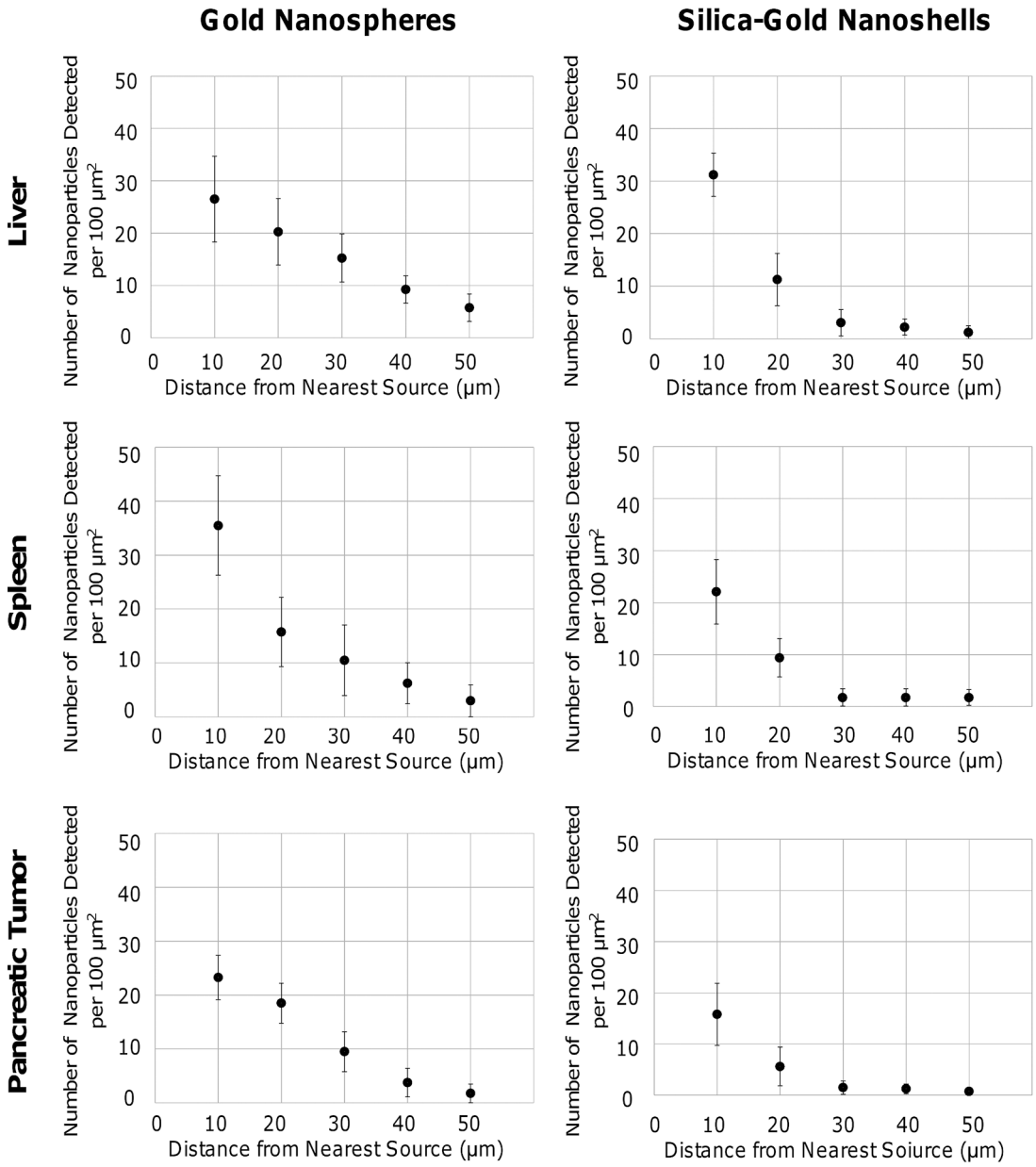

Fig. 5. Penetration of PC-coated gold NPs in liver, spleen, and pancreatic tumor tissues [70]. Particles were visualized using hyperspectral imaging, and their distances measured from nearest source points. In the liver and pancreatic tumor, gold nanospheres had linear diffusion, while in the spleen it was an exponential decline. Silica gold nanoshells had an exponential decline for all tissue types, suggesting limited diffusivity. Their extravasation was highest in the liver, while for gold nanospheres it was highest in the spleen. All error bars denote standard deviation ($n = 3$). Reprinted from England *et al.*, *PLoS One* **10**, e0129172 (2015); used in accordance with Creative Commons Attribution (CC BY) license.

mathematical modeling and computational simulation have been applied to complement the empirical effort in order to gain further insight into these phenomena. Nanotherapeutic response can be simulated by describing tumors as physical objects subject to physical laws, such as conservation of mass and momentum. Extensive modeling work studying tumor growth as well as angiogenesis has been published in recent years, as reviewed in [119–137] and associated references, with a subset of studies focusing on nanotherapy [24,27,138–148]. For example, the interaction between NP vascular extravasation, uptake, and distribution with heterogeneous tumor interstitial, vascular, and lymphatic conditions was studied in [140], finding that an elevated interstitial hydraulic conductivity leads to low NP accumulation regardless of NP capacity for vascular extravasation. The results further showed that an elevated

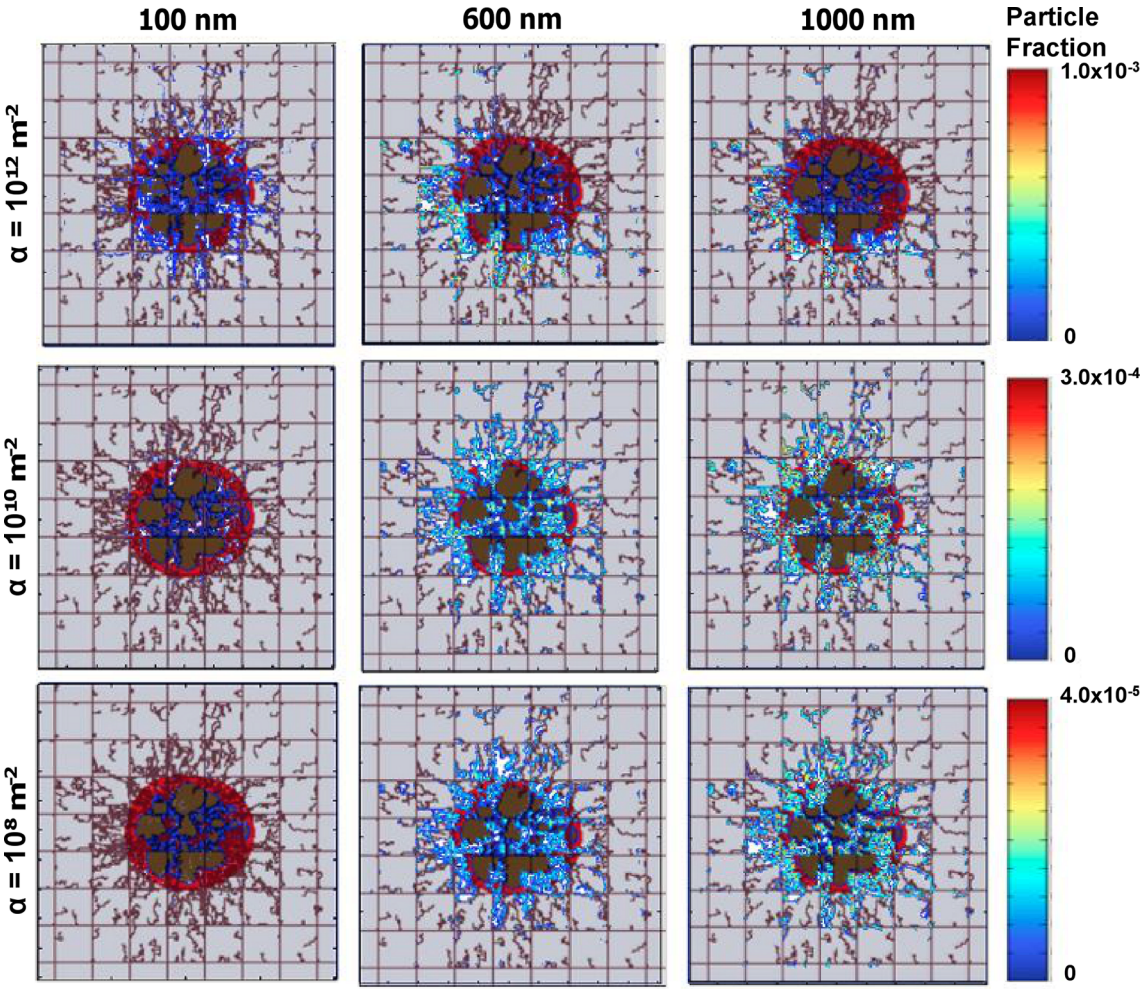

Fig. 6. Example of computational modeling to assess generic NP uptake in heterogeneously vascularized tumor tissue [139]. The columns denote three different NP sizes (100, 600, and 1000 nm), while the rows denote three different values for the model parameter α, related to NP vascular affinity. The color scale provides a measure of fraction of injected NPs adhering at blood vessel walls at ~ 100 minutes after injection upstream of the tumor mass (bottom left corner in each panel). The tumor lesions ($\sim 750\,\mu$m diameter) have distinct regions denoting viable, hypoxic, and necrotic tissue, respectively represented by red, blue, and brown colors. Pre-existing capillary vessels, shown as straight lines, are laid out in a regular grid establishing normoxic conditions in the surrounding tissue. Angiogenesis-induced capillaries (irregular lines) sprout from the pre-existing vessels in response to pro-angiogenic factors produced by the hypoxic tissue. Field of view is 2×2 mm. Reprinted from Frieboes *et al.*, *PLoS One* **8**, e56876 (2013); used in accordance with Creative Commons Attribution (CC BY) license.

vascular hydraulic conductivity modulates NP accumulation in a manner inversely proportional to the capacity for extravasation.

Some modeling studies have examined how tissue biological factors, including tumor size and vascularity, as well as NP physiochemical properties, such as size and surface modifications, affect NP performance [27,139,140,143,147,149]. The models may provide insight into NP uptake and distribution *in vivo*, which could help define NP and therapy parameters. In particular, a mathematical model was developed in [143] to predict NP diffusive transport and spatial distribution in 3D cell culture representing under-vascularized tissue, based on NP parameters measured from monolayer cell culture including diffusivity, cell surface binding capacity, and rate constants of association, dissociation, and cellular internalization. In [142], *in vitro* experiments were combined with mathematical modeling to study the synergistic effect of nanoparticle geometry (size, shape) and molecular targeting on specificity of delivery to tumor vasculature. An integrated approach was proposed in [144] for the rational design of NPs for intravascular delivery of imaging contrast agents and therapeutics. The approach combines *in vitro* experiments and *in vivo* intravital microscopy (IVM) with mathematical modeling to identify combinations of NP size, shape, and surface properties that maximize nanoparticle uptake within diseased vasculature.

The transport and accumulation of NPs targeted to tumor vasculature has recently been modeled based on size, surface density and molecular affinity of surface ligands, and the expression of surface receptors on tumor endothe-

lium [139]. The simulations showed that with higher vascular affinity, smaller NPs (100 nm) exhibited a more uniform distribution within tumor tissue, while larger NPs (600 and 100 nm) distributed inhomogeneously as their larger size with increased vascular affinity hindered their diffusivity (fig. 6). In contrast, smaller NPs with lower vascular affinity did not accumulate in the tumor. Low vascular affinity for larger NPs increased their accumulation and more homogeneous distribution. Optimal distribution and uptake were achieved for medium vascular affinity and intermediate-sized particles (600 nm), for which vascular and receptor affinity synergistically combined to yield higher accumulation and more homogeneous distribution [139].

Conclusion

We have reviewed recent work studying the uptake and distribution of gold NPs in solid tumors, and examined in detail the performance of gold nanospheres and nanoshells in tissue *in vitro* and *in vivo*. The goal of these efforts is to evaluate how gold NP design in terms of size and surface modifications can help to overcome transport barriers in the tumor microenvironment in order to improve nanotherapy efficacy, and thus ultimately improve patient outcomes. Results *in vivo* illustrate the sequestering by the RES, with a high concentration of NPs uptaken in the spleen and the liver. Smaller gold NPs overall had enhanced tumor tissue accumulation compared to larger NPs. Functionalization of gold NPs has been shown to possibly improve targeting, transport, and uptake. As would be expected, low tissue vascularization hinders NP uptake regardless of size, *e.g.*, as in pancreatic tumors [70].

3D cell culture offers the possibility to study diffusion into under-vascularized tumor tissue, as occurs locally in tumors. As reviewed here, the uptake and distribution of NPs within avascular/hypoxic regions of solid tumors has been studied using such *in vitro* models [69,70,99]. However, tissue within live subjects is more complex than that formed in 3D cell culture, typically having a fully developed ECM and multiple cell types (including immune system cells) in proximity of blood and lymph vessels, which may affect the deposition patterns and uptake of NPs beyond the mere effects of diffusion in 3D space. NP extravasation in tumor tissue *in vivo* is affected by interstitial fluid pressure, as evidenced in experimental and modeling studies [22,32,140]. The RES and other systemic factors *in vivo* may also significantly affect NP performance beyond what can be discerned from these experimental models.

Electron microscopy techniques (TEM, SEM, STEM) have traditionally been employed to detect NPs in tissue samples [150]. Other techniques including confocal microscopy have also been employed to assess NP translocation in co-culture cancer models [151]. Newer NP detection methodologies present opportunities for improved detection. In particular, hyperspectral imaging has shown the feasibility of determining particle size, wavelength differentiation, spatial location, and agglomeration status of NPs in solution [152]. In [70,99], dark-field microscopy in combination with hyperspectral imaging was used to evaluate NP uptake and distribution within tissue samples harvested from mice.

Further elucidation of gold NP uptake and distribution in tumor tissue could advance the potential for photothermal and targeted drug delivery therapies [153], as well as novel diagnostic imaging techniques such as multispectral optoacoustic tomography (MSOT) [154–157]. In combination with mathematical modeling, the experimental efforts could thus provide a suitable progression towards systematic development of more effective cancer nanotherapy.

References

1. L. Aschoff, K. Kiyono, Folia Haematol. **15**, 383 (1913).
2. W.H. De Jong, P.J.A. Borm, Int. J. Nanomed. **3**, 133 (2008).
3. Z. Zhang, J. Chen, L. Ding *et al.*, Small **6**, 430 (2010).
4. J. Wang, Z. Lu, Y. Gao, M.G. Wientjes, J.L.S. Au, Nanomedicine **6**, 1605 (2011).
5. S.D. Li, L. Huang, Biochim. Biophys. Acta-Biomembr. **1788**, 2259 (2009).
6. L. Zhang, F.X. Gu, J.M. Chan, A.Z. Wang, R.S. Langer, O.C. Farokhzad, Clinical Pharmacol. Therapeutics **83**, 761 (2008).
7. H. Schellekens, W.E. Hennink, V. Brinks, Pharm. Res. **30**, 1729 (2013).
8. G.H. Algire, H.W. Chalkley, J. Nat. Cancer Inst. **6**, 73 (1945).
9. E. Goldman, Lancet **2**, 1236 (1907).
10. A.G. Ide, N.H. Baker, S.L. Warren, Am. J. Radiol. **42**, 891 (1939).
11. M. Greenblatt, P. Shubik, J. Natl. Cancer Inst. **41**, 111 (1968).
12. R.L. Ehrmann, M. Knoth, J. Natl. Cancer Inst. **41**, 1329 (1968).
13. D.R. Senger, S.J. Galli, A.M. Dvorak, C.A. Perruzzi, V.S. Harvey, H.F. Dvorak, Science **219**, 983 (1983).
14. F. Yuan, M. Dellian, D. Fukumura *et al.*, Cancer Res. **55**, 3752 (1995).
15. H. Hashizume, P. Baluk, S. Morikawa *et al.*, Am. J. Pathol. **156**, 1363 (2000).
16. G. Kong, R.D. Braun, M.W. Dewhirst, Cancer Res. **60**, 4440 (2000).
17. S.K. Libutti, G.F. Paciotti, A.A. Byrnes *et al.*, Clin. Cancer Res. **16**, 6139 (2010).
18. Y. Matsumura, H. Maeda, Cancer Res. **46**, 6387 (1986).
19. H. Maeda, Adv. Enzyme Regul. **41**, 189 (2001).

20. C.J. Murphy, A.M. Gole, J.W. Stone *et al.*, Acc. Chem. Res. **41**, 1721 (2008).
21. W.C. Zamboni, V. Torchilin, A.K. Patri *et al.*, Clin. Cancer Res. **18**, 3229 (2012).
22. R.K. Jain, T. Stylianopoulos, Nat. Rev. Clin. Oncol. **7**, 653 (2010).
23. B.A. Chabner, *Cancer Chemotherapy and Biotherapy: Principles and Practice*, 5th edition (Lippincott Williams & Wilkins, Philadelphia, PA, 2011).
24. A.L. van de Ven, M. Wu, J. Lowengrub *et al.*, AIP Adv. **2**, 11208 (2012).
25. I. Brigger, C. Dubernet, P. Couvreur, Adv. Drug Delivery Rev. **54**, 631 (2002).
26. R.K. Jain, Cancer Res. **47**, 3039 (1987).
27. A.L. van de Ven, B. Abdollahi, C.J. Martinez *et al.*, New J. Phys. **15**, 55004 (2013).
28. R.A. Cairns, I.S. Harris, T.W. Mak, Nat. Rev. Cancer **11**, 85 (2011).
29. M. Vinci, S. Gowan, F. Boxall *et al.*, Bmc Biol. **10**, 29 (2012).
30. B.L. Krock, N. Skuli, M.C. Simon, Genes Cancer **2**, 1117 (2011).
31. N. Raghunand, R.A. Gatenby, R.J. Gillies, Br. J. Radiol. **76**, S11 (2003).
32. L.T. Baxter, R.K. Jain, Microvasc. Res. **37**, 77 (1989).
33. L.T. Baxter, R.K. Jain, Microvasc. Res. **40**, 246 (1990).
34. J. Conde, F.R. Tian, Y. Hernandez *et al.*, Biomaterials **34**, 7744 (2013).
35. R. Bhat, V.G. Sharanabasava, R. Deshpande, U. Shetti, G. Sanjeev, A. Venkataraman, J. Photochem. Photobiol. B-Biology **125**, 63 (2013).
36. M. Liu, X.H. Gu, K. Zhang *et al.*, J. Nanoparticle Res. **15**, 1745 (2013).
37. Y.J. Choi, Y.J. Kim, J.W. Lee *et al.*, J. Nanosci. Nanotechnol. **13**, 4437 (2013).
38. H.W. Kao, Y.Y. Lin, C.C. Chen *et al.*, Bioorg. Med. Chem. Lett. **23**, 3180 (2013).
39. F. Ren, S. Bhana, D.D. Norman *et al.*, Bioconjug. Chem. **24**, 376 (2013).
40. O. Fellahi, R.K. Sarma, M.R. Das *et al.*, Nanotechnology **24**, 495101 (2013).
41. R. Sankar, A. Karthik, A. Prabu, S. Karthik, K.S. Shivashangari, V. Ravikumar, Colloids Surf. B-Biointerfaces **108**, 80 (2013).
42. R.M. Gengan, K. Anand, A. Phulukdaree, A. Chuturgoon, Colloids Surf. B-Biointerfaces **105**, 87 (2013).
43. R. Govender, A. Phulukdaree, R.M. Gengan, K. Anand, A.A. Chuturgoon, J. Nanobiotechnol. **11**, 5 (2013).
44. K.M. Vyas, R.N. Jadeja, D. Patel, R.V. Devkar, V.K. Gupta, Polyhedron **65**, 262 (2013).
45. R. Magaye, J.S. Zhao, L. Bowman, M. Ding, Exp. Ther. Med. **4**, 551 (2012).
46. M.C. Thounaojam, R.N. Jadeja, M. Valodkar, P.S. Nagar, R.V. Devkar, S. Thakore, Food Chemical Toxicol. **49**, 2990 (2011).
47. S. Kankala, R.K. Kankala, R. Balaboina, N.S. Thirukovela, R. Vadde, C.S. Vasam, Bioorg. Med. Chem. Lett. **24**, 1180 (2014).
48. J. Zhang, Y. Fu, Y. Mei, F. Jiang, J.R. Lakowicz, Anal Chem **82**, 4464 (2010).
49. R. Wan, Y. Mo, S. Chien *et al.*, Nanotoxicology **5**, 568 (2011).
50. E.E. Glista-Baker, A.J. Taylor, B.C. Sayers, E.A. Thompson, J.C. Bonner, Am. J. Respir. Cell Mol. Biol. **47**, 552 (2012).
51. M. Ahamed, M.J. Akhtar, H.A. Alhadlaq *et al.*, Chemosphere **135**, 278 (2015).
52. W. Cai, T. Gao, H. Hong, J. Sun, Nanotechnol. Sci. Appl. **2008**, 17 (2008).
53. L. Dykman, N. Khlebtsov, Chem. Soc. Rev. **41**, 2256 (2012).
54. X. Huang, M.A. El-Sayed, J. Adv. Res. **1**, 13 (2010).
55. N. Garrett, M. Whiteman, J. Moger, Opt. Express **19**, 17563 (2011).
56. Z.S. Liang, Y. Liu, X.Y. Li *et al.*, J. Biomed. Mater. Res. Part A **98A**, 479 (2011).
57. B.D. Chithrani, A.A. Ghazani, W.C.W. Chan, Nano Lett. **6**, 662 (2006).
58. A.M. Alkilany, C.J. Murphy, J. Nanoparticle Res. **12**, 2313 (2010).
59. L.C. Kennedy, L.R. Bickford, N.A. Lewinski *et al.*, Small **7**, 169 (2011).
60. M. Tang, P.J. Russell, A. Khatri, Discov. Med. **7**, 68 (2007).
61. M. Wang, N.O. Petersen, Biochim. Biophys. Acta **1831**, 1089 (2013).
62. G. Peng, U. Tisch, O. Adams *et al.*, Nat Nano **4**, 669 (2009).
63. O. Barash, N. Peled, U. Tisch, P.A. Bunn, Jr., F.R. Hirsch, H. Haick, Nanomedicine **8**, 580 (2012).
64. S.J. Oldenburg, R.D. Averitt, S.L. Westcott, N.J. Halas, Chem. Phys. Lett. **288**, 243 (1998).
65. F.Y. Cheng, C.T. Chen, C.S. Yeh, Nanotechnology **20**, 425104 (2009).
66. H.Y. Liu, D. Chen, F.Q. Tang *et al.*, Nanotechnology **19**, 455101 (2008).
67. A.R. Lowery, A.M. Gobin, E.S. Day, N.J. Halas, J.L. West, Int. J. Nanomed. **1**, 149 (2006).
68. A.M. Gobin, M.H. Lee, N.J. Halas, W.D. James, R.A. Drezek, J.L. West, Nano Lett. **7**, 1929 (2007).
69. C.G. England, T. Priest, G. Zhang *et al.*, Int. J. Nanomed. **8**, 3603 (2013).
70. C.G. England, J. Kurtis, J. Huang, X. Zhang, A.M. Gobin, H.B. Frieboes, PLoS One **10**, e0129172 (2015).
71. G. Frens, Nat. Phys. Sci. **241**, 20 (1973).
72. W. Vogel, D.G. Duff, A. Baiker, Langmuir **11**, 401 (1995).
73. T.C. Preston, R. Signorell, ACS Nano **3**, 3696 (2009).
74. W. Stöber, A. Fink, E. Bohn, J. Colloid Interface Sci. **26**, 62 (1968).
75. H. Takahashi, Y. Niidome, T. Niidome, K. Kaneko, H. Kawasaki, S. Yamada, Langmuir **22**, 2 (2006).
76. S. Huo, H. Ma, K. Huang *et al.*, Cancer Res. **73**, 319 (2013).
77. C.D. Bain, H.A. Biebuych, G.M. Whitesides, Langmuir **5**, 723 (1989).

78. H. Häkkinen, Nat. Chem. **4**, 443 (2012).
79. C.G. England, T. Priest, G. Zhang *et al.*, Int. J. Nanomed. **8**, 3603 (2013).
80. J. Kimling, M. Maier, B. Okenve, V. Kotaidis, H. Ballot, A. Plech, J. Phys. Chem. B **110**, 15700 (2006).
81. L. Shang, K. Nienhaus, G.U. Nienhaus, J. Nanobiotechnol. **12**, 5 (2014).
82. E.A. Sykes, J. Chen, G. Zheng, W.C. Chan, ACS Nano **8**, 5696 (2014).
83. K. Leung, *Gold-polyethylene glycol nanoshells*, in *Molecular Imaging and Contrast Agent Database (MICAD)* (NCBI, Bethesda, MD, 2004).
84. D.P. O'Neal, L.R. Hirsch, N.J. Halas, J.D. Payne, J.L. West, Cancer Lett. **209**, 171 (2004).
85. J.V. Jokerst, T. Lobovkina, R.N. Zare, S.S. Gambhir, Nanomedicine (London) **6**, 715 (2011).
86. T. Maldiney, C. Richard, J. Seguin, N. Wattier, M. Bessodes, D. Scherman, ACS Nano **5**, 854 (2011).
87. X. Gu, W. Zhang, J. Liu *et al.*, AAPS Pharm. Sci. Tech. **12**, 1200 (2011).
88. S. Wen, F. Zheng, M. Shen, X. Shi, J. Appl. Polym. Sci. **128**, 3807 (2013).
89. B.A. Lewis, D.M. Engelman, J. Mol. Biol. **166**, 211 (1983).
90. J.F. Nagle, S. Tristram-Nagle, Biochim. Biophys. Acta **1469**, 159 (2000).
91. K. El Harchaoui, B.J. Arsenault, R. Franssen *et al.*, Ann. Intern. Med. **150**, 84 (2009).
92. J. Zheng, K. Nagashima, D. Parmiter, J. de la Cruz, A.K. Patri, Methods Mol. Biol. **697**, 93 (2011).
93. K. Sokolov, M. Follen, J. Aaron *et al.*, Cancer Res. **63**, 1999 (2003).
94. P.H. Yang, X. Sun, J.F. Chiu, H. Sun, Q.Y. He, Bioconj. Chem. **16**, 494 (2005).
95. J.M. de la Fuente, C.C. Berry, M.O. Riehle, A.S.G. Curtis, Langmuir **22**, 3286 (2006).
96. I.H. El-Sayed, X. Huang, M.A. El-Sayed, Nano Lett. **5**, 829 (2005).
97. D. Boyer, P. Tamarat, A. Maali, B. Lounis, M. Orrit, Science **297**, 1160 (2002).
98. J.F. Hainfeld, M.J. O'Connor, F.A. Dilmanian, D.N. Slatkin, D.J. Adams, H.M. Smilowitz, Br. J. Radiol. **84**, 526 (2011).
99. D. Yohan, C. Cruje, X. Lu, D. Chithrani, Nano-Micro Lett. **7**, 127 (2015).
100. P. Zarogoulidis, K. Darwiche, L. Krauss *et al.*, Future Oncol. **9**, 1307 (2013).
101. S.O. Jeon, H.J. Hwang, D.H. Oh *et al.*, J. Microencapsulat. **29**, 234 (2012).
102. K. Darwiche, P. Zarogoulidis, L. Krauss *et al.*, Int. J. Nanomed. **8**, 4533 (2013).
103. A.S. Goldsborough, M.D. Handley, A.E. Dulcey, K.M. Pluchino, P. Kannan, K.R. Brimacombe, J. Med. Chem. **54**, 4987 (2011).
104. J.A. Dahl, B.L. Maddux, J.E. Hutchison, Chem. Rev. **107**, 2228 (2007).
105. A. Kumar, H. Ma, X. Zhang *et al.*, Biomaterials **33**, 1180 (2012).
106. B.D. Chithrani, A.A. Ghazani, W.C. Chan, Nano Lett. **6**, 662 (2006).
107. J.A. Kim, C. Aberg, A. Salvati, K.A. Dawson, Nat. Nanotechnol. **7**, 62 (2012).
108. C.L. Walte, C.M. Roth, Bioconj. Chem. **20**, 1908 (2009).
109. C.L. Walte, C.M. Roth, Biotechnol. Bioeng. **108**, 2999 (2011).
110. T.T. Goodman, P.L. Olive, S.H. Pun, Int. J. Nanomed. **2**, 265 (2007).
111. K. Huang, H. Ma, J. Liu *et al.*, ACS Nano **6**, 4483 (2012).
112. J.C. Yen, F.J. Chang, S. Chang, IEEE Trans Image Process **4**, 370 (1995).
113. C. Wong, T. Stylianopoulos, J.A. Cui *et al.*, Proc. Natl. Acad. Sci. U.S.A. **108**, 2426 (2011).
114. V.P. Chauhan, T. Stylianopoulos, J.D. Martin *et al.*, Nat. Nanotechnol. **7**, 383 (2012).
115. S. Hirn, M. Semmler-Behnke, C. Schleh *et al.*, Eur. J. Pharm. Biopharm. **77**, 407 (2011).
116. J.F. Hainfeld, D.N. Slatkin, T.M. Focella, H.M. Smilowitz, Br. J. Radiol. **79**, 248 (2006).
117. E. Sadauskas, H. Wallin, M. Stoltenberg *et al.*, Part. Fibre Toxicol. **4**, 10 (2007).
118. C.R. Patra, R. Bhattacharya, E.F. Wang *et al.*, Cancer Res. **68**, 1970 (2008).
119. Z. Wang, J.D. Butner, V. Cristini, T.S. Deisboeck, J. Pharmacokinet. Pharmacodyn. **42**, 179 (2015).
120. T.S. Deisboeck, Z. Wang, P. Macklin, V. Cristini, Annu. Rev. Biomed. Eng. **13**, 127 (2011).
121. Z. Wang, T.S. Deisboeck, Drug Discov. Today **19**, 145 (2014).
122. J. Bachmann, A. Raue, M. Schilling, V. Becker, J. Timmer, U. Klingmuller, J. Int. Med. **271**, 155 (2012).
123. V. Andasari, A. Gerisch, G. Lolas, A.P. South, M.A. Chaplain, J. Math. Biol. **63**, 141 (2011).
124. M.A.J. Chaplain, Ima J. Appl. Math. **76**, 371 (2011).
125. F. Michor, J. Liphardt, M. Ferrari, J. Widom, Nat. Rev. Cancer **11**, 657 (2011).
126. K.A. Rejniak, A.R.A. Anderson, WIREs Syst. Biol. Med. **3**, 115 (2011) DOI: 10.1002/wsbm.102.
127. K.R. Swanson, R.C. Rockne, J. Claridge, M.A. Chaplain, E.C. Alvord, A.R.A. Anderson, Cancer Res. **71**, 7366 (2011).
128. H.B. Frieboes, M.A. Chaplain, A.M. Thompson, E.L. Bearer, J.S. Lowengrub, V. Cristini, Cancer Res. **71**, 298 (2011).
129. H.M. Byrne, Nat. Rev. Cancer **10**, 221 (2010).
130. P.K. Kreeger, D.A. Lauffenburger, Carcinogenesis **31**, 2 (2010).
131. K.A. Rejniak, L.J. McCawley, Exp. Biol. Med. **235**, 411 (2010).
132. J.S. Lowengrub, H.B. Frieboes, F. Jin *et al.*, Nonlinearity **23**, R1 (2010).
133. P. Vineis, A. Schatzkin, J.D. Potter, Carcinogenesis **31**, 1703 (2010).
134. J.M. Osborne, A. Walter, S.K. Kershaw *et al.*, Philos. Trans. R. Soc. A-Math. Phys. Engin. Sci. **368**, 5013 (2010).
135. L.B. Edelman, J.A. Eddy, N.D. Price, WIREs Syst. Biol. Med. **2**, 438 (2010).
136. A. Palladini, G. Nicoletti, F. Pappalardo *et al.*, Cancer Res. **70**, 7755 (2010).
137. V. Cristini, J. Lowengrub, *Multiscale modeling of cancer: an integrated experimental and mathematical modeling approach* (Cambridge University Press, 2010).

138. C.D. Kaddi, J.H. Phan, M.D. Wang, Nanomedicine (London) **8**, 1323 (2013).
139. H.B. Frieboes, M. Wu, J. Lowengrub, P. Decuzzi, V. Cristini, PloS One **8**, e56876 (2013).
140. M. Wu, H.B. Frieboes, M.A. Chaplain, S.R. McDougall, V. Cristini, J. Lowengrub, J. Theor. Biol. **355**, 194 (2014).
141. M. Li, J. Reineke, Int. J. Nano Biomater. **3**, 222 (2011).
142. P. Decuzzi, R. Pasqualini, W. Arap, M. Ferrari, Pharm. Res. **26**, 235 (2009).
143. Y. Gao, M. Li, B. Chen *et al.*, AAPS J **15**, 816 (2013).
144. B. Godin, W.H. Driessen, B. Proneth *et al.*, Adv. Genetics **69**, 31 (2010).
145. H.B. Frieboes, J.P. Sinek, O. Nalcioglu, J.P. Fruehauf, V. Cristini, *Nanotechnology in Cancer Drug Therapy: A Biocomputational Approach*, in *BioMEMS and Biomedical Nanotechnology*, edited by M. Ferrari, A.P. Lee, L.J. Lee (Springer, US, 2006) p. 435.
146. M. Li, Z. Panagi, K. Avgoustakis, J. Rineke, Int. J. Nanomed. **7**, 1345 (2012).
147. M. Li, K.T. Al-Jamal, K. Kostarelos, J. Reineke, ACS Nano **4**, 6303 (2010).
148. M. Li, E.A. Czyszczon, J.J. Reineke, Drug Deliv. Transl. Res. **3**, 551 (2013).
149. M. Li, J. Reineke, Methods Mol. Biol. **926**, 369 (2012).
150. P.J. Kempen, A.S. Thakor, C. Zavaleta, S.S. Gambhir, R. Sinclair, Microsc. Microanal. **19**, 1290 (2013).
151. P.M. Costa, A.L. Cardoso, L.S. Mendonca *et al.*, Mol. Ther. Nucleic Acids **2**, e100 (2013).
152. H. Weinkauf, B.F. Brehm-Stecher, Biotechnol. J. **4**, 871 (2009).
153. L.C. Kennedy, L.R. Bickford, N.A. Lewinski *et al.*, Small **7**, 169 (2011).
154. C.S. Guo, S. Yin, H.J. Yu *et al.*, Nanoscale **5**, 6469 (2013).
155. Y. Li, W. Lu, Q. Huang, M. Huang, C. Li, W. Chen, Nanomedicine (London) **5**, 1161 (2010).
156. A. Taruttis, E. Herzog, D. Razansky, V. Ntziachristos, Opt. Express **18**, 19592 (2010).
157. T. Grosges, D. Barchiesi, S. Kessentini, G. Grehan, M.L. de la Chapelle, Biomed. Opt. Express **2**, 1584 (2011).